3. Larson, R. B. Thermal physics, cloud geometry and the stellar initial mass function. *Mon. Not. R. Astron. Soc.* **359,** 211–222 (2005).
4. Bonnell, I. A., Bate, M. R. & Zinnecker, H. On the formation of massive stars. *Mon. Not. R. Astron. Soc.* **298,** 93–102 (1998).
5. Bonnell, I. A., Bate, M. R., Clarke, C. J. & Pringle, J. E. Competitive accretion in embedded stellar clusters. *Mon. Not. R. Astron. Soc.* **323,** 785–794 (2001).
6. Bonnell, I. A., Clarke, C. J., Bate, M. R. & Pringle, J. E. Accretion in stellar clusters and the initial mass function. *Mon. Not. R. Astron. Soc.* **324,** 573–579 (2001).
7. Bonnell, I. A., Vine, S. G. & Bate, M. R. Massive star formation: nurture, not nature. *Mon. Not. R. Astron. Soc.* **349,** 735–741 (2004).
8. Bate, M. R. & Bonnell, I. A. The origin of the initial mass function and its dependence on the mean Jeans mass in molecular clouds. *Mon. Not. R. Astron. Soc.* **356,** 1201–1221 (2005).
9. Bate, M. R., Bonnell, I. A. & Bromm, V. The formation mechanism of brown dwarfs. *Mon. Not. R. Astron. Soc.* **332,** L65–L68 (2002).
10. Bate, M. R., Bonnell, I. A. & Bromm, V. The formation of a star cluster: predicting the properties of stars and brown dwarfs. *Mon. Not. R. Astron. Soc.* **339,** 577–599 (2003).
11. Mohanty, S., Jayawardhana, R. & Basri, G. The T Tauri phase down to nearly planetary masses: echelle spectra of 82 very low mass stars and brown dwarfs. *Astrophys. J.* **626,** 498–522 (2005).
12. Krumholz, M. R., McKee, C. F. & Klein, R. I. Bondi-Hoyle accretion in a turbulent medium. *Astrophys. J.* (in the press); preprint at (http://arXiv.org/astro-ph/0510410) (2005).
13. McKee, C. F. & Tan, J. C. The formation of massive stars from turbulent cores. *Astrophys. J.* **585,** 850–871 (2003).
14. Padoan, P., Kritsuk, A., Norman, M. L. & Nordlund, Å. A solution to the pre-main-sequence accretion problem. *Astrophys. J. Lett.* **622,** L61–L64 (2005).
15. Bertoldi, F. & McKee, C. F. Pressure-confined clumps in magnetized molecular clouds. *Astrophys. J.* **395,** 140–157 (1992).
16. Fiege, J. D. & Pudritz, R. E. Helical fields and filamentary molecular clouds—I. *Mon. Not. R. Astron. Soc.* **311,** 85–104 (2000).
17. Edgar, R. & Clarke, C. The effect of radiative feedback on Bondi-Hoyle flow around a massive star. *Mon. Not. R. Astron. Soc.* **349,** 678–686 (2004).
18. Ruffert, M. & Arnett, D. Three-dimensional hydrodynamic Bondi-Hoyle accretion. 2. Homogeneous medium at mach 3 with $\gamma = 5/3$. *Astrophys. J.* **427,** 351–376 (1994).
19. Larson, R. B. Turbulence and star formation in molecular clouds. *Mon. Not. R. Astron. Soc.* **194,** 809–826 (1981).
20. Motte, F., Andre, P. & Neri, R. The initial conditions of star formation in the ρ Ophiuchi main cloud: wide-field millimeter continuum mapping. *Astron. Astrophys.* **336,** 150–172 (1998).
21. Testi, L. & Sargent, A. I. Star formation in clusters: A survey of compact millimeter-wave sources in the Serpens core. *Astrophys. J. Lett.* **508,** L91–L94 (1998).
22. Johnstone, D., Fich, M., Mitchell, G. F. & Moriarty-Schieven, G. Large area mapping at 850 microns. III. Analysis of the clump distribution in the Orion B molecular cloud. *Astrophys. J.* **559,** 307–317 (2001).
23. Plume, R., Jaffe, D. T., Evans, N. J., Martin-Pintado, J. & Gomez-Gonzalez, J. Dense gas and star formation: Characteristics of cloud cores associated with water masers. *Astrophys. J.* **476,** 730–749 (1997).
24. Klessen, R. S. & Burkert, A. The formation of stellar clusters: gaussian cloud conditions I. *Astrophys. J. Suppl.* **128,** 287–319 (2000).
25. Klessen, R. S. & Burkert, A. The formation of stellar clusters: gaussian cloud conditions II. *Astrophys. J.* **549,** 386–401 (2001).
26. Bate, M. R., Bonnell, I. A. & Bromm, V. The formation of close binary systems by dynamical interactions and orbital decay. *Mon. Not. R. Astron. Soc.* **336,** 705–713 (2002).
27. Beuther, H. & Schilke, P. Fragmentation in massive star formation. *Science* **303,** 1167–1169 (2004).
28. Quillen, A. C. *et al.* Turbulence driven by outflow-blown cavities in the molecular cloud of NGC 1333. *Astrophys. J.* (in the press); preprint at (http://arXiv.org/astro-ph/0503167) (2005).
29. Cho, J. & Lazarian, A. Compressible magnetohydrodynamic turbulence: mode coupling, scaling relations, anisotropy, viscosity-damped regime and astrophysical implications. *Mon. Not. R. Astron. Soc.* **345,** 325–339 (2003).
30. Kramer, C. & Winnewisser, G. A molecular survey of the dark cloud L 1495 in Taurus. *Astron. Astrophys. Suppl.* **89,** 421–428 (1991).

Supplementary Information is linked to the online version of the paper at www.nature.com/nature.

Acknowledgements We thank R. T. Fisher for discussions and P. Padoan for comments. This work was supported by grants from NASA through the Hubble Fellowship, GSRP and ATP programmes, by the NSF, and by the US DOE through the Lawrence Livermore National Laboratory. Computer simulations for this work were performed at the San Diego Supercomputer Center (supported by the NSF), the National Energy Research Scientific Computer Center (supported by the US DOE), and Lawrence Livermore National Laboratory (supported by the US DOE). M.R.K. is a Hubble Fellow.

Author Information Reprints and permissions information is available at npg.nature.com/reprintsandpermissions. The authors declare no competing financial interests. Correspondence and requests for materials should be addressed to M.R.K. (krumholz@astro.princeton.edu).

LETTERS

Nanofabricated media with negative permeability at visible frequencies

A. N. Grigorenko[1], A. K. Geim[1], H. F. Gleeson[1], Y. Zhang[1], A. A. Firsov[1,2], I. Y. Khrushchev[3] & J. Petrovic[3]

A great deal of attention has recently been focused on a new class of smart materials—so-called left-handed media—that exhibit highly unusual electromagnetic properties and promise new device applications[1–6]. Left-handed materials require negative permeability μ, an extreme condition that has so far been achieved only for frequencies in the microwave to terahertz range[7–11]. Extension of the approach described in ref. 7 to achieve the necessary high-frequency magnetic response in visible optics presents a formidable challenge[12–15], as no material—natural or artificial—is known to exhibit any magnetism at these frequencies. Here we report a nanofabricated medium consisting of electromagnetically coupled pairs of gold dots with geometry carefully designed at a 10-nm level. The medium exhibits a strong magnetic response at visible-light frequencies, including a band with negative μ. The magnetism arises owing to the excitation of an antisymmetric plasmon resonance. The high-frequency permeability qualitatively reveals itself via optical impedance matching. Our results demonstrate the feasibility of engineering magnetism at visible frequencies and pave the way towards magnetic and left-handed components for visible optics.

Landau and Lifshitz argued[12] "there is certainly no meaning in using the magnetic susceptibility from optical frequencies onwards, and in discussion of such phenomena we must put $\mu = 1$". This statement is strongly supported by experiment: the magnetic susceptibility χ of all natural materials tails off at microwave frequencies. Still, there may be a way to overcome the fundamental limitations, as shown by Pendry *et al.* who have suggested exploiting the inductive response from structured non-magnetic materials to obtain high-frequency magnetism[7]. The idea was successfully implemented by using arrays of copper split-rings that generated a magnetic response at frequencies up to 100 THz (refs 8–11). In this case, magnetic properties emerge owing to collective motion of a large number of electrons, and theoretical arguments (as, for example, in ref. 12) valid for individual electrons and atoms no longer hold. It is tempting to extend the approach further to visible-light frequencies, where one can expect most applications. However, the direct scaling of the demonstrated microwave media to visible optics is problematic. This would require split-ring-like structures with sizes down to 100 nm and critical features[8–11] controlled on the level of ~10 nm, which is technologically difficult to achieve. More importantly, the scaling could fail in principle because of different electromagnetic responses of materials to visible light and microwaves (for example, it was predicted that inherent losses should limit the approach demonstrated in refs 7–11 to frequencies well below optical[13,15]).

In this work, by employing a novel geometry, we make a critical step of demonstrating metamaterials with magnetic response at frequencies in the visible spectrum. The design of our media follows recent theoretical suggestions[14,15], and relies on antisymmetric plasmon resonances in a simple pair of short metal pillars of a submicrometre size (Fig. 1). The simplification of the resonator geometry with respect to the double split-rings geometry used in microwaves is important for two reasons. First, this allows the use of current lithography techniques to fabricate metallic structures with plasmon resonances at visible-light frequencies. Second, the simple geometry reduces the number of resonant modes interacting with a light field, which consequently leads to a reduction in energy losses. Note that such changes in geometry also reflect the trend known from lasing techniques, where complex closed resonators used in masers were replaced by simple open resonators (pair of mirrors) in lasers[16,17].

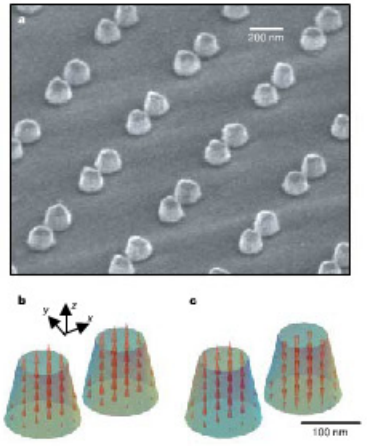

Figure 1 | Nanofabricated medium with magnetic response at optical frequencies. a, Scanning electron micrograph (viewed at an angle) of an array of Au nanopillars. **b**, **c**, Numerical simulation of the distribution of electric currents (arrows) inside a pair of such pillars for the symmetric and antisymmetric resonant *z*-modes, respectively. The non-cylindrical shape of pillars is important to provide an efficient coupling to incident light, and was intentionally introduced in our design through a choice of microfabrication procedures.

[1]Department of Physics and Astronomy, University of Manchester, Manchester, M13 9PL, UK. [2]Institute of Microelectronics Technology, 142432 Chernogolovka, Russia. [3]Department of Electronic Engineering, Aston University, Aston Triangle, Birmingham B4 7ET, UK.

Figure 1 shows an example of our devices and illustrates the basic idea behind the experiment. The prepared structures were large arrays of Au pillars fabricated by high-resolution electron-beam lithography on a glass substrate and grouped in tightly spaced pairs (except for reference samples consisting of similar but isolated Au pillars). The structures typically covered an area of ~0.1 mm^2 and contained ~10^6 pillars. The lattice constant, a, for periodic arrays was down to 400 nm—that is, smaller than the wavelength λ of visible light. Heights h of Au pillars (80–90 nm) and their diameters $d \approx 100$ nm were chosen through numerical simulations so that the plasmon resonance in the reference samples appeared at red-light wavelengths, $\lambda \approx 670$ nm. A number of different structures were studied with d between 80 nm and 140 nm and the pair separation s between centres of adjacent pillars in the range 140 nm to 200 nm; that is, the gap $s - d$ between the neighbouring pillars varied from 100 nm down to almost zero. (The best results were achieved at $s = 200$ nm, $d = 140$ nm, $h = 80$ nm, and $s = 140$ nm, $d = 110$ nm, $h = 90$ nm.) At these separations, electromagnetic interaction between neighbouring pillars within a pair is important and plasmon resonance observed for an individual pillar splits into two resonances for a pillar pair. These resonances are referred to as symmetric and antisymmetric, similar to the case of any classical or quantum system with two interacting parts and in agreement with the notation used for plasmon resonances in nanoparticles[18].

There exist three symmetric and three antisymmetric main resonant modes in an interacting pair with currents flowing along the x, y and z axes. Figure 1 shows the symmetric (Fig. 1b) and the antisymmetric (Fig. 1c) z-modes calculated for our experimental geometry using Femlab software (Comsol Inc.). For the symmetric resonance, electrons in neighbouring pillars move in phase and generate overall a dipole contribution to permittivity ε, similar to isolated or non-interacting pillars. In the antisymmetric z-mode, however, electrons move in anti-phase so that the oscillating dipoles cancel each other leaving only magnetodipole and quadrupole responses[19]. One can see in Fig. 1c that the anti-phase movement of electrons along the z axis effectively results in a current loop in the z–x plane (note that a pair of pillars can be thought of as a ring with two slits at the opposite sides). This high-frequency electric current generates a magnetic moment in the y-direction and contributes to permeability μ. Not all resonant modes are necessarily excited by incident light. Modes' coupling to light is governed by the symmetry group of a pillar pair, which is C_{2v} in our case. For this group, normal incident light with the electric field along the x axis (later referred to as TM polarization) is coupled to both the dipole symmetric x-mode and the magnetic antisymmetric z-mode, while normal light with the electric field along the y axis (TE polarization) excites only the dipole symmetric y-mode, as discussed in ref. 20. The choice of the symmetry group is important for creating magnetic response (for example, magnetic modes are not necessarily excited in a pair of infinite cylinders with the symmetry group C_{2h}; ref. 21).

The symmetry of our pillar pairs thus implies that an array of pillar pairs should exhibit two main plasmon resonances (z-antisymmetric and x-symmetric) for TM light of normal incidence, one of which (z-antisymmetric) disappears and the other (x-symmetric) changes into y-symmetric resonance as we rotate polarization by 90°, to TE polarization. On the other hand, an array of isolated pillars should demonstrate only one resonance for both polarizations. Our experiments confirmed this. Figure 2 shows the reflection spectra measured in normal incident light of TM and TE polarizations (green and red curves, respectively) for arrays made of pillar pairs of the same dimensions but different lattice constants, as well as for the reference array of isolated pillars (micrographs of the corresponding samples are shown next to their spectra.) The reference array exhibits only one resonance at $\lambda \approx 670$ nm for both polarizations (Fig. 2g and h), in agreement with our symmetry and numerical analyses. On the other hand, arrays made of the same pillars but packed in interacting pairs showed two distinct resonances in the TM spectra (Fig. 2a, c and e). If the polarization of incident light was rotated by 90°, the high-frequency, 'green' resonance disappeared, and the reflection spectra showed only the low-frequency, 'red' resonance, albeit with its position slightly shifted (Fig. 2b, d and f). The change in the reflection spectra was so marked that the colour of the samples viewed in white light changed (see photographs in Fig. 2). Our structures looked amber for TE light, similar in colour to the media consisting of isolated pillars. In stark contrast, for TM polarization, the structures look green owing to a large contribution from the green resonance.

The spectral positions of red and green resonance peaks did not depend on the lattice constant for all studied samples with pillar pairs of the same dimensions (Fig. 2c and e shows two examples with $a = 400$ and 600 nm). This excludes diffraction as a possible origin for the observed resonances. This was further confirmed by making random arrays of pillar pairs, which did not influence the spectral positions of the resonance peaks. (It is worth noting that, contrary to our case, diffraction modes play a prominent role in light reflection from perforated metal[22] or arrays of nanoparticles deposited on metallic substrates[23].) Although the resonance positions did not depend on a, they were strongly affected by changing separation s and by covering the structure with a dielectric medium, as expected for resonances split by electromagnetic interaction between pillars. As an example, Fig. 2a and b shows reflection spectra of the same sample as in Fig. 2c and d but covered by an optically thin (<30 nm) layer of glycerine. This resulted in a notable red-shift of the green resonance peak by $\delta\lambda \approx 50$ nm, in agreement with red-shifts

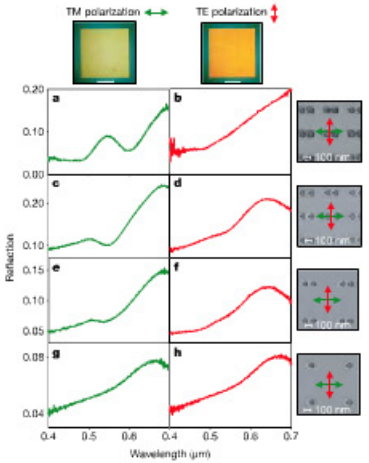

Figure 2 | Experimental reflection spectra for our nanostructured media. Green and red curves are for TM and TE polarizations of normal incident light, respectively. Micrographs of the studied samples are shown on the right. For all the samples, pillars have the same separation $s = 140$ nm, height $h = 90$ nm and average diameter $d = 110$ nm. Spectra **a**, **b**, are for the sample of **c**, **d**, but covered with an optically thin layer of glycerine; for **c**, **d**, the lattice constant $a = 400$ nm; for **e**, **f**, $a = 600$ nm; **g**, **h**, are for isolated pillars with $a = 600$ nm. The top photographs show images of the sample **a**, **b**, in white light for two polarizations.

reported for multipole resonances in nanoparticles[24]. Moreover, we observed a significant increase (by a factor of 3) in the strength of the green resonance. Note that, in this case, the structure reflected as much as 10% of light near the green resonance peak (Fig. 2a), which is a significant magnitude under our experimental conditions (for comparison, a glass substrate with $\varepsilon = 2.25$ reflects only 4% of the incident light).

The described experiments assign the green-light resonance (disappearing in TE polarization) unambiguously to the antisymmetric z-mode, which gives rise to μ, and the red-light resonances to the x- and y-symmetric modes, contributing to ε (refs 14, 15). To further strengthen this identification of the resonances, we compare the measured spectra with theory (Fig. 3). The theoretical calculations were performed with the Electromagnetic module of Femlab software, which solves Maxwell's equations for the actual experimental geometry. We described pillars by Drude's conductivity

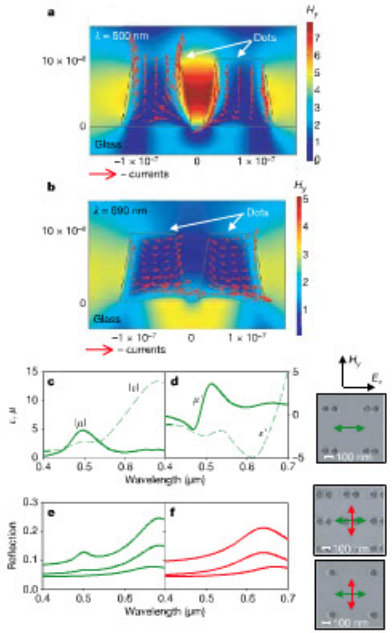

Figure 3 | Numerical simulations of optical response for interacting Au pillars. **a**, **b**, Distribution of electric currents (red arrows) and magnetic field H_y (colour map measured in units of the magnetic field amplitude of the incident wave) for the pillars being illuminated by normal incident light of TM polarization with wavelengths $\lambda = 500$ nm (**a**) and $\lambda = 690$ nm (**b**). Geometrical sizes are shown in metres at the bottom and the left of images. 'Dots' in the image refer to Au nanopillars. **c**, **d**, The spectral dependence of permittivity ε and permeability μ; **c** shows the absolute values and **d** the real parts. **e**, **f**, Calculated reflection spectra corresponding to the experimental situation in Fig. 2.

$\sigma(\omega) = \sigma_0/(1 - i\omega\tau)$, where ω is the angular frequency of light, $\sigma_0 = 3.7 \times 10^{17}\ s^{-1}$ the conductivity of gold and $\tau = 2.4 \times 10^{-14}$ s the scattering time, and the glass substrate by a dielectric with permittivity $\varepsilon = 2.25$. The calculations have confirmed that TM green light of normal incidence with $\lambda = 500$ nm excites anti-phase currents flowing mostly along the z axis (Fig. 3a), which is a characteristic of the antisymmetric z-mode. A current loop is effectively created in the z–x plane, which generates strong magnetic fields H_y in the region between pillars (the red region of Fig. 3a) and produces a substantial magnetic moment. On the other hand, TM red light at $\lambda = 690$ nm excites mostly in-phase currents flowing along the x axis, which do not produce any significant magnetic moment (Fig. 3b).

We have also calculated the spectral dependence of effective permeability and permittivity of our structures. Figure 3 shows the absolute values and real parts for ε_x and μ_y (denoted here as ε and μ) for the tightest pair packing (the curves were obtained by solving Maxwell's equations for an electromagnetic wave interacting with a periodic array on top of a glass substrate). The calculated spectral positions of the peaks in ε and μ are in good agreement with the peak positions found experimentally, and the theoretical reflection spectra also agree well with the experimental data. The calculations show that our microstructures have considerable permeability $\mu' = \mathrm{Re}(\mu)$ ranging from −1 to 3 for the array of tightest packing (Fig. 3d). For the sample of Fig. 2c, for example, its calculated permeability varied between 0.5 and 1.5, and for Fig. 2a μ' varied between −0.25 and 2.1.

As a complementary analysis to the numerical simulations, we have employed another approach that is routinely used in optics to extract material parameters from reflection spectra[25,26]. To this end, we noted that, neglecting mode interaction, the calculated resonances in permittivity followed the standard dispersion relation[25] $\Delta\varepsilon(\lambda) = f_\varepsilon\lambda^2/(\lambda^2 - \lambda_\varepsilon^2 - i\lambda\Delta\lambda_\varepsilon)$, where λ_ε is the wavelength of the symmetric resonance, $\Delta\lambda_\varepsilon$ its half-width and f_ε the effective oscillator

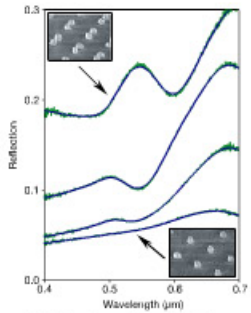

Figure 4 | Example of fitting the experimental reflection spectra with theory. The green curves are the measured spectra of Fig. 2; the blue curves show the best fit based on the dispersion relations described in the main text. The parameters of the main resonances extracted from the fitting curves are as follows. Single pillars: $\lambda_x \approx 665$ nm, $\Delta\lambda_x \approx 165$ nm and $f_x \approx 0.79$. Pairs with $a = 600$ nm: $\lambda_x \approx 690$ nm, $\Delta\lambda_x \approx 147$ nm, $f_x \approx 1.76$ and $\lambda_y \approx 550$ nm, $\Delta\lambda_y \approx 85$ nm, $f_y \approx 0.06$. Pairs with $a = 400$ nm: $\lambda_x \approx 685$ nm, $\Delta\lambda_x \approx 147$ nm, $f_x \approx 3.27$ and $\lambda_x \approx 552$ nm, $\Delta\lambda_x \approx 80$ nm, $f_x \approx 0.16$. Pairs covered with a glycerine film: $\lambda_x \approx 710$ nm, $\Delta\lambda_x \approx 140$ nm, $f_x \approx 1.7$ and $\lambda_x \approx 598$ nm, $\Delta\lambda_x \approx 80$ nm, $f_x \approx 0.32$. The spectrum of the sample covered with a glycerine film is offset for clarity. The insets show micrographs of the corresponding samples.

strength. The spectral dependence of calculated permeability is also described well by the 'Pendry-type' expression[7,10] $\mu(\lambda) = 1 + f_a\lambda_a^2/(\lambda^2 - \lambda_a^2 - i\lambda\Delta\lambda_a)$, where λ_a, $\Delta\lambda_a$ and f_a are the same notations as above but for the antisymmetric resonance (see Supplementary Information for details). The combination of these dispersion relations with the Fresnel's reflection coefficients for a thin anisotropic film placed on a glass substrate[25,26] leads to relatively simple expressions that can be used to fit the experimental spectra and find ε and μ. For example, in the case of Fig. 2c, the best fit to its spectra yields $\chi' \approx -0.5$ ($\mu' \approx 0.5$) near $\lambda = 470$ nm and corroborates the results of the Fernlab calculations (see Fig. 4). Similarly, the spectra for the samples covered with a glycerine film and showing an increased strength in the antisymmetric resonance yielded a significant increase in $|\chi|$, such that negative values of μ' were achieved almost routinely. For example, χ' was about -1.3 at the green resonance in Fig. 2a (that is, $\mu' \approx -0.3$). Although our structures exhibited both negative μ' and negative ε' within the same range of λ (for example, $\varepsilon' \approx -0.7$ and $\mu' \approx -0.3$ at the green resonance in Fig. 2a), μ had a rather large imaginary component ($\mu'' \equiv \mathrm{Im}(\mu) \approx 1i$ at the resonance), which so far has not allowed the observation of negative refraction.

We have however observed another effect—optical impedance matching—that is more tolerant to dissipation but also exclusive to materials with a finite permeability. The effect of impedance matching is characterized by the total suppression of reflection from an interface between two media with different refraction indices, $n = (\varepsilon\mu)^{1/2}$, but the same impedance values, $Z = (\varepsilon/\mu)^{1/2}$. This impedance matching is well known for electrical and microwave circuits but was never observed for conventional optics, because it requires $\mu \neq 1$ (except for singular cases of optical waveguides[27]), which has been unachievable until now. In our case, this phenomenon resulted in a total invisibility of our structured films at green-resonance frequencies for TM polarization of incident light, while the films could still be seen by using phase contrast imaging or TE polarization. For brevity, the experiments are described in Supplementary Information.

Received 19 May; accepted 19 September 2005.

1. Veselago, V. G. The electrodynamics of substances with simultaneously negative values of permittivity and permeability. *Sov. Phys. Usp.* **10**, 509–514 (1968).
2. Pendry, J. B. Negative refraction makes a perfect lens. *Phys. Rev. Lett.* **85**, 3966–3969 (2000).
3. Shelby, R. A., Smith, D. R. & Schultz, S. Experimental verification of a negative index of refraction. *Science* **292**, 77–79 (2001).
4. Smith, D. R., Padilla, W. J., Vier, D. C., Nemat-Nasser, S. C. & Schultz, S. Composite medium with simultaneously negative permeability and permittivity. *Phys. Rev. Lett.* **84**, 4184–4187 (2000).
5. Pendry, J. B. Positively negative. *Nature* **423**, 22–23 (2003).
6. Houck, A. A., Brock, J. B. & Chuang, I. L. Experimental observations of a left-handed material that obeys Snell's law. *Phys. Rev. Lett.* **90**, 137401 (2003).
7. Pendry, J. B., Holden, A. J., Robbins, D. J. & Stewart, W. J. Magnetism from conductors and enhanced nonlinear phenomena. *IEEE Trans. Microwave Theory Tech.* **47**, 2075–2084 (1999).
8. Wiltshire, M. C. K. *et al.* Microstructured magnetic materials for RF flux guides in magnetic resonance imaging. *Science* **291**, 849–851 (2001).
9. Pendry, J. B. & O'Brien, S. Magnetic activity at infrared frequencies in structured photonic crystals. *J. Phys. Condens. Matter* **14**, 6383–6394 (2002).
10. Yen, T. J. *et al.* Terahertz magnetic response from artificial materials. *Science* **303**, 1494–1496 (2004).
11. Linden, S. *et al.* Magnetic response of metamaterials at 100 terahertz. *Science* **306**, 1351–1353 (2004).
12. Landau, L. D. & Lifshitz, E. M. *Electrodynamics of Continuous Media* Section 60 (Oxford, Pergamon, 1960).
13. Dimmock, J. O. Losses in left-handed materials. *Opt. Express* **11**, 2397–2402 (2003).
14. Panina, L. V., Grigorenko, A. N. & Makhnovskiy, D. P. Metal-dielectric medium with conducting nanoelements. *Phys. Rev. B* **66**, 155411 (2002).
15. Podolskiy, V. A., Sarychev, A. K. & Shalaev, V. M. Plasmon modes in metal nanowires and left-handed materials. *J. Nonlinear Opt. Phys. Mater.* **11**, 65–74 (2002).
16. Prokhorov, A. M. Molecular amplifier and generator for submillimeter waves. *Zh. Eksp. Teor. Fiz.* **34**, 1658–1659 (1958).
17. Schawlow, A. L. & Townes, C. H. Infrared and optical masers. *Phys. Rev.* **112**, 1940–1949 (1958).
18. Aizpurua, J. *et al.* Optical properties of gold nanorings. *Phys. Rev. Lett.* **90**, 057401 (2003).
19. Jin, R. *et al.* Controlling anisotropic nanoparticle growth through plasmon excitation. *Nature* **425**, 487–490 (2003).
20. Barron, L. D. *Molecular Light Scattering and Optical Activity* (Cambridge Univ. Press, Cambridge, UK, 1982).
21. Kottmann, J. P. & Martin, O. J. F. Plasmon resonant coupling in metallic nanowires. *Opt. Express* **8**, 655–663 (2001).
22. Ebbesen, T. W., Lezec, H. J., Ghaemi, H. F., Thio, T. & Wolff, P. A. Plasmon-assisted transmission of entangled photons. *Nature* **391**, 667–669 (1998).
23. Feldj, N. *et al.* Enhanced substrate-induced coupling in two-dimensional gold nanoparticle arrays. *Phys. Rev. B* **66**, 245407 (2002).
24. Mock, J. J., Smith, D. R. & Schultz, S. Local refractive index dependence of plasmon resonance spectra from individual nanoparticles. *Nano Lett.* **3**, 485–491 (2003).
25. Born, M. & Wolf, E. *Principles of Optics* Section 2.3 (Cambridge Univ. Press, Cambridge, UK, 1980).
26. Abeles, F. in *Physics of Thin Films* Vol. 6 (eds Francombe, M. H. & Hoffman, R. W.) Ch. V–VII (Academic, New York, 1971).
27. Gademann, A., Durkan, C. & Shvets, I. V. Optical impedance matching with near-field optical microscopy. *J. Phys. D* **36**, 2193–2197 (2003).

Supplementary Information is linked to the online version of the paper at www.nature.com/nature.

Acknowledgements This research was supported by EPSRC (UK). We thank L. Panina and D. Makhnovskiy for discussions, and N. Roberts for collaboration in experiments. A.A.F. acknowledges support from INTAS.

Author Information Reprints and permissions information is available at npg.nature.com/reprintsandpermissions. The authors declare no competing financial interests. Correspondence and requests for materials should be addressed to A.N.G. (sasha@iman.ac.uk).

LETTERS

Spin-torque diode effect in magnetic tunnel junctions

A. A. Tulapurkar[1,2]†, Y. Suzuki[1,2,3], A. Fukushima[1,2], H. Kubota[1,2], H. Maehara[4], K. Tsunekawa[4], D. D. Djayaprawira[4], N. Watanabe[4] & S. Yuasa[1,2]

There is currently much interest in the development of 'spintronic' devices, in which harnessing the spins of electrons (rather than just their charges) is anticipated to provide new functionalities that go beyond those possible with conventional electronic devices. One widely studied example of an effect that has its roots in the electron's spin degree of freedom is the torque exerted by a spin-polarized electric current on the spin moment of a nanometre-scale magnet. This torque causes the magnetic moment to rotate[1–14] at potentially useful frequencies. Here we report a very different phenomenon that is also based on the interplay between spin dynamics and spin-dependent transport, and which arises from unusual diode behaviour. We show that the application of a small radio-frequency alternating current to a nanometre-scale magnetic tunnel junction[15–22] can generate a measurable direct-current (d.c.) voltage across the device when the frequency is resonant with the spin oscillations that arise from the spin-torque effect: at resonance (which can be tuned by an external magnetic field), the structure exhibits different resistance states depending on the direction of the current. This behaviour is markedly different from that of a conventional semiconductor diode[23], and could form the basis of a nanometre-scale radio-frequency detector in telecommunication circuits.

We performed experiments on a magnetic tunnel junction (MTJ) in the structure Si (substrate)/PtMn (15 nm)/CoFe (2.5 nm)/Ru (0.85 nm)/CoFeB (3 nm)/MgO (0.85 nm)/CoFeB (3 nm); see Fig. 1a. This multi-layered film was further patterned into oval-shaped pillars of dimension 200 nm × 100 nm, using electron-beam lithography and ion milling techniques. The bottom anti-ferromagnetically coupled CoFe and CoFeB layers (the synthetic antiferromagnetic layer) act as a pinned layer, while the top CoFeB layer acts as a free layer, whose magnetization can be changed. The resistance of the MTJ depends on the relative orientations of the pinned and free layers. The present MTJ shows a giant tunnelling magnetoresistance (TMR) due to the crystalline MgO (001) tunnelling barrier. A current passing through the MTJ gets spin-polarized by the pinned layer, and exerts a torque on the free layer.

The experimental arrangement to measure the diode effect is shown in Fig. 1a. A bias T is used to pass high-frequency current (200 MHz to 15 GHz) through the MTJ and to measure the d.c. voltage simultaneously. For all the experiments described here, the external magnetic field was applied at an angle of 30° from the pinned-layer magnetization axis within the film plane (see inset of Fig. 1b). In this geometry the sample showed a giant TMR of ~100%, as shown in Fig. 1b. We also measured microwave power from the MTJ arising from the thermal fluctuations of the free-layer magnetization[14,15]. The power was measured by a spectrum analyser, by passing a d.c. current of 1 mA using a bias T.

The radio frequency (r.f.) response of the MTJ was first tested using a network analyser. The results obtained showed evidence of magnetic resonance excited by r.f. current (results not shown).

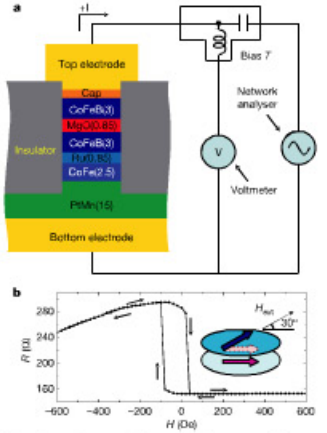

Figure 1 | Experimental set-up and magnetoresistance. a, Schematic diagram of the experimental set-up and cross-sectional view of the magnetic tunnel junction (MTJ) device. The thicknesses of various layers of the device in nanometres are given in brackets. The bottom CoFeB and CoFe layers, coupled anti-ferromagnetically through the Ru layer, act as a pinned layer. The top CoFeB layer acts as a free layer, the magnetization of which can be changed. The pinned and free layers are separated by a tunnelling MgO barrier. The experimental set-up measures the d.c. voltage produced across the device on applying the r.f. current. **b**, The magnetoresistance of the device, by applying magnetic field at 30° from the pinned-layer magnetization. The arrows indicate the sweeping direction of the magnetic field.

†Nanoelectronics Research Institute, National Institute of Advanced Industrial Science and Technology (AIST), Tsukuba 305-8568, Japan. ‡CREST, Japan Science and Technology Agency (JST), 4-1-8 Honcho, Kawaguchi 332-0012, Japan. §Graduate School of Engineering Science, Osaka University, 1-3 Machikaneyama, Toyonaka, Osaka 560-8531, Japan. ‖Electron Device Equipment Division, Canon ANELVA Corporation, 5-8-1 Yotsuya, Fuchu, Tokyo 183-8508, Japan. ¶Present address: Stanford Linear Accelerator Center, Stanford University, California 94025, USA.